


Propagating intrinsic localized mode in a cyclic, dissipative, self-dual one-dimensional nonlinear transmission line

M. Sato¹,* H. Furusawa¹, and Y. Soga¹*Graduate School of Natural Science and Technology, Kanazawa University, Kanazawa, Ishikawa 920-1192, Japan*A. J. Sievers²*Laboratory of Atomic and Solid State Physics, Cornell University, Ithaca, New York 14853-2501, USA*
 (Received 30 August 2022; revised 2 February 2023; accepted 14 February 2023; published 7 March 2023)

A well-known feature of a propagating localized excitation in a discrete lattice is the generation of a backwave in the extended normal mode spectrum. To quantify the parameter-dependent amplitude of such a backwave, the properties of a running intrinsic localized mode (ILM) in electric, cyclic, dissipative, nonlinear 1D transmission lines, containing balanced nonlinear capacitive and inductive terms, are studied via simulations. Both balanced and unbalanced damping and driving conditions are treated. The introduction of a unit cell duplex driver, with a voltage source driving the nonlinear capacitor and a synchronized current source, the nonlinear inductor, provides an opportunity to design a cyclic, dissipative self-dual nonlinear transmission line. When the self-dual conditions are satisfied, the dynamical voltage and current equations of motion within a cell become the same, the strength of the fundamental, resonant coupling between the ILM and the lattice modes collapses, and the associated fundamental backwave is no longer observed.

DOI: [10.1103/PhysRevE.107.034202](https://doi.org/10.1103/PhysRevE.107.034202)

I. INTRODUCTION

Although a dissipative nonlinear transmission line (NLTL) is necessarily a nonconservative system, it is often used to compare experimental findings [1–17] with lattice solitons [18–21], discrete breathers [22–24], or intrinsic localized mode (ILM) [25–30] expectations. The properties of such strongly localized excitations in NLTLs have been described in a number of reviews [31–40]. A desired solitonlike property, such as the distortionless, free motion of a running energy pulse, is an important goal, but one impediment for the running ILM is the seemingly intrinsic backwave generated in the discrete nonlinear lattice [41–44]. For a mechanical one-dimensional (1D) NLTL, it is well-known that the ILM site-centered and bond-centered locations in the unit cell have different energies and this imbalance associated with a traveling ILM excites NLTL modes [45–48]. The fundamental challenge is how best to uncouple a running ILM from the NLTL extended-wave excitations in a dissipative lattice, where a driver is required to maintain the nonlinear ILM in the steady state. For NLTLs without damping, a few ways have been suggested to decrease the lattice-ILM interaction: a saturable nonlinearity [49,50], the balance of two different kinds of lattice nonlinearities [44], by including odd symmetry potential terms [51], or with a symmetrically designed set of long-range potentials [52]. But without accounting for intrinsic loss, such NLTL proposals remain conjectural. For ILMs in driven-dissipative NLTLs, there have been some studies [39,53–56] but the focus has not been on how to

control the magnitude of the NLTL backwave generated by a running ILM.

In this paper, using simulations with cell drivers, damping, and building on our earlier experimental ILM-NLTL studies [17], we examine the representative properties of a running ILM in a 32 element, electric-cyclic, driven-damped, nonlinear transmission line. Here we demonstrate, first with a traveling-wave (voltage) driver (model 1) and then with a balanced, traveling wave, duplex (voltage, current) driver (model 2), the different ILM-lattice coupling properties for equalized nonlinearities in NLTLs. Each of these models is tested with balanced and unbalanced damping. Particularly interesting in our paper is model (2), for the case where all components in such a basically realistic nonlinear unit cell are balanced, the result is a damped, self-dual NLTL. It is demonstrated here that unlike for a single cell (voltage) driver, the balanced-duplex (voltage, current) driver makes possible the removal of the backward NLTL wave associated with the fundamental resonant coupling between the ILM and the lattice. The result is a nearly free running ILM.

In the next section, we provide some background details based on earlier works [17,44] to set the stage for the findings to follow. The self-dual NLTL equations are developed in Sec. III. A number of steps are involved. First, the balanced nonlinearities are presented, then the unit cell duplex driver characterized, and, finally, the dynamic equations of motion for the NLTL quantified. In Sec. IV, the running ILM simulation results are presented. They detail exactly how best to suppress a specific fundamental backwave resonance, both for a single driver and for a duplex driver. As a final point, it is demonstrated that there is no fundamental backwave

*msato153@staff.kanazawa-u.ac.jp

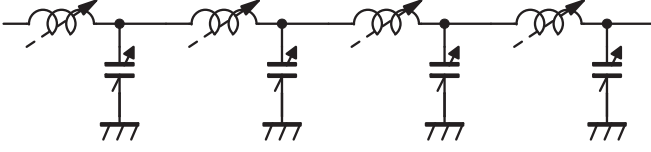


FIG. 1. Ideal cyclic nonlinear transmission line. The unit cell consists of a single hard nonlinear capacitor, a single hard nonlinear inductor, and no dissipation.

resonance for a running ILM in such a self-dual NLTL. The summary and conclusions follow in Sec. V.

II. BACKGROUND

A. Unit cell for cyclic NLTL

Electrical experiments, using a cyclic 32-element NLTL with hard nearest neighbor nonlinearity and a voltage traveling-wave driver in each cell, already have been used to generate and observe running ILMs over a wide range of driver frequency and wavenumber. The basic cyclic electrical configuration is shown in Fig. 1, where the particular case of interest is for the unit cell capacitor and inductor to have different nonlinearities. At small excitation amplitude the well-known linear dispersion curve of the NLTL is given by

$$\omega(k) = \frac{2}{\sqrt{L_0 C_0}} \sin \left| \frac{k}{2} \right|, \quad (1)$$

where ω is the frequency, k is the wave number, L_0 is the linear inductance, and C_0 , the linear capacitance. The propagating, wave-driving pattern is

$$V_{d,n} = V_d \cos(k_d n - \omega_d t), \quad (2)$$

where n is the lattice index and V_d , k_d and ω_d are the driving amplitude, wave number, and frequency, respectively.

An illustration, presenting the dispersion properties of NLTL and an ILM, is given in Fig. 2. The linear dispersion curve for the NLTL is shown by the solid red curve. For the case of hard nearest-neighbor nonlinearity, with neighboring

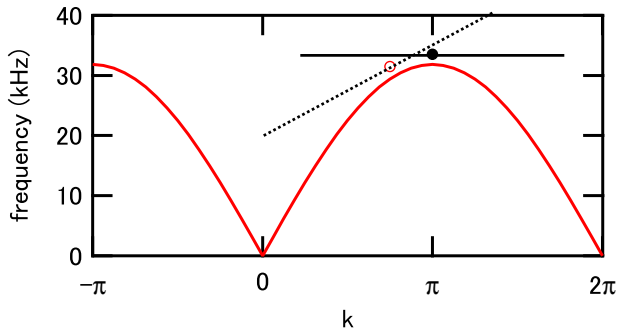


FIG. 2. 2D-FT schematic drawing of stationary and traveling ILMs superimposed on the solid NLTL dispersion curve. Solid and open circles indicate driving points for stationary and traveling ILMs, respectively. An ILM is expressed as a dispersion line (DL) in k space because it is a localized wave packet in physical space. The solid horizontal line is for a stationary ILM, while the dashed sloped line is for an ILM traveling to the right.

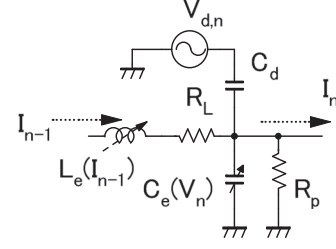


FIG. 3. One unit cell of the experimental cyclic NLTL with different $C_e(V)$ and $L_e(I)$ nonlinearities. R_p is the parallel resistor of the capacitor, R_L is the series resistor of the inductor, and $V_{d,n}$ the voltage driver with driving capacitor C_d .

cells excited π out of phase with each other, a stationary ILM can be generated above the NLTL dispersion curve maximum. In Fig. 2, the solid black dot identifies the frequency and wave number driver of such an ILM. The horizontal line represents the range of the two-dimensional (2D) Fourier transform (FT) of (time, site) for the ILM amplitude distribution in k space. (See Appendix for FT details.) The sharper this stationary ILM in physical space, the broader the 2D-FT representation of the mode in k space. For the range where $0 < k < \pi$, the open circle in Fig. 2 identifies the frequency and wave number driver of a traveling ILM, and the dotted dispersion line (DL) of the ILM, its distribution in k space. This particular ILM is traveling to the right and the slope shown is directly related to the ILM speed around the ring. From this picture, it should be evident that for a running ILM its DL will always intersect the NLTL dispersion curve. This intersection point of the dotted curve and the red curve identifies the resonance location between the wing of the ILM FT amplitude and the NLTL dispersion curve. It was found that the ILM velocity depends on the amplitude of this resonance, among other parameters, and that the ILM-induced NLTL backwave can be easily recognized in the spectrum [17].

The schematic electrical design of an actual NLTL unit cell for the case of a traveling-wave voltage driver is presented in Fig. 3. Here C_e is the differential nonlinear capacitance, L_e is the differential nonlinear inductance, R_p is the parallel resistor, representing dissipation in the nonlinear capacitor, and R_L is the series resistor representing loss in the nonlinear inductor. Both resistance terms are included to account for damping in the circuit. To capacitively drive the unit cell, one end of the nonlinear capacitor (voltage node V_n) is connected to the unit cell, driving oscillator through a linear capacitor C_d , which increases the total capacitance of the nonlinear capacitance from C_e to $C_e + C_d$.

B. Experimental ILM-NLTL resonance observation

We now have all the components necessary to determine experimentally the resonance feature from a running ILM 2-D FT (time, site) data set. An experimentally measured example of the position versus time of a running ILM is shown in Fig. 4(a). The blue (maximum), white (zero), and red (minimum) track versus time identifies the measured voltage pattern of a running ILM for a particular cyclic NLTL. As mentioned above, by taking the 2D FT of these voltage data (see Appendix), one obtains the DL for the ILM, as shown

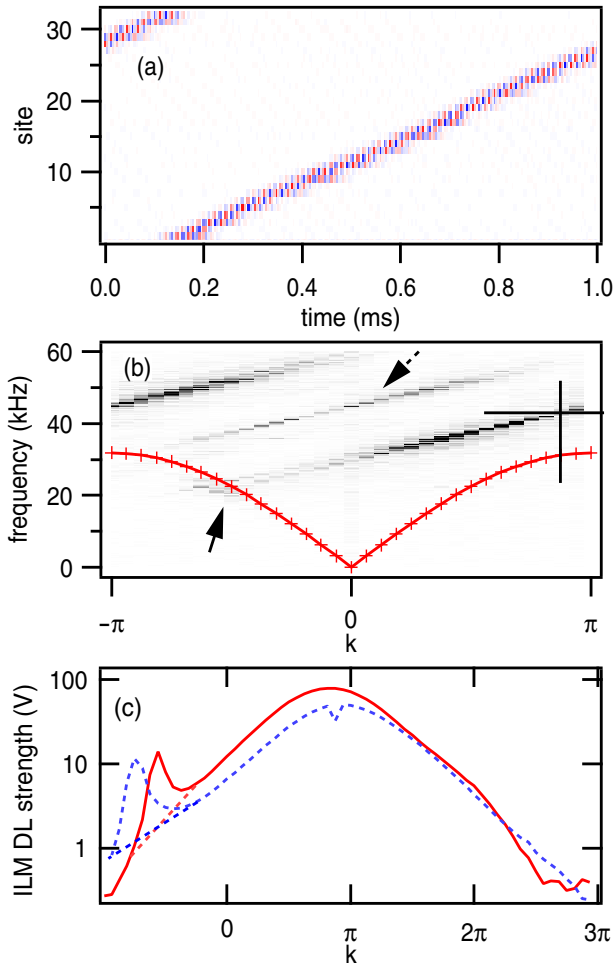


FIG. 4. Comparison of experimental and simulation ILM resonance properties. (a) Experimental voltage pattern versus time for a traveling ILM in a capacitor driven nonlinear transmission line. (b) 2D-FT result of the voltage pattern in (a) gives the ILM dispersion line strength (DLS). Solid red curve indicates the NLTL linear dispersion curve. Cross identifies driver wavenumber $14\pi/16$ and driver frequency 43 kHz. The ILM DL intersects the NLTL dispersion curve at the solid arrow. (Signal at middle, dashed arrow, is an experimental ghost.) (c) Solid curve: ILM DLS versus wave number. Dashed curve is obtained from a simulation with the same conditions as the experiment. Long dashed curves beneath the resonances give approximate baselines.

in Fig. 4(b). The cross identifies the particular traveling-wave driver settings (frequency and wave number). The frequency versus wave number DL density plot identifies the modulus voltage amplitude (V) of the ILM, the darker the gray scale, the larger the DL modulus amplitude. The slope of the ILM DL is the ILM velocity per unit lattice constant divided by 2π . The continuation of the DL modulus amplitude into the next zone is shown on the left-hand side of this figure. It is clear that the voltage density extends all the way to the NLTL dispersion curve (see solid arrow) and beyond.

To examine the resonance crossing in more details, the procedure is to obtain a measure of the magnitude of ILM-DL density as it varies across the Brillouin zone. To obtain the dispersion line strength (DLS) at a specific k value the

magnitude is summed over a small frequency range. See Appendix, Eq. (A3). This DLS (V) is shown as a function of wave number in Fig. 4(c) where the log of the resulting strength is graphed versus wave number. As expected, the maximum value occurs at the position of the driving location cross in the previous panel. Initially, the DLS drops off as one moves away from this k -space location until the resonance location between the ILM and the NLTL appears. Superimposed on the same panel, the blue dotted curve gives the corresponding simulation results for the same set of NLTL parameters. Notice that the curves are similar but the resonance interaction is even stronger than observed in experiments. This observation is consistent with the fact that the simulated ILM travels at a slower speed than does the experimentally observed ILM. It has also been found that by setting equal the magnitudes of the nonlinear inductor and the nonlinear capacitor in simulations the resonant interaction can be greatly reduced, although a significant component remains. In the next section, basically starting from this last observation, we continue the exploration of how best to minimize this resonant interaction between a running-localized excitation and the extended waves in a NLTL.

III. DEVELOPMENT OF SELF-DUAL NLTL

A. Model 1, balanced nonlinearities

To study with simulations the properties of the NLTL leading to the self-dual case, the first step along this path is to balance the two nonlinearities in the unit cell. For the studies described in this paper, the unit cell nonlinear capacitor is set equal to the nonlinear inductor, so

$$\frac{L_e(V/Z_0)}{L_0} = \frac{C_e(V)}{C_0}, \quad (3)$$

where $Z_0 = \sqrt{L_0/C_0}$. Equation (3) is now applied throughout our paper. The differential capacitance C_e is the same inverse hyperbolic function of the voltage as in Ref. [17], namely,

$$C_e(V) = \frac{C_0}{\sqrt{1 + V^2/V_0^2}}, \quad (4)$$

where C_0 and V_0 are constants. For the inductor, the differential inductance L_e is taken to have the same structure, so

$$L_e(I) = \frac{L_0}{\sqrt{1 + I^2/I_0^2}}, \quad (5)$$

where L_0 and I_0 are constants. Note, although most nonlinear inductors show a parabolic current dependence for $1/L_e$ instead of hyperbolic, it is not hard to generate Eq. (5) since the desired model dependence can be synthesized by adding together several inductors with different current dependencies. When these parameters satisfy the energy relation

$$C_0V_0^2 = L_0I_0^2, \quad (6)$$

the nonlinear capacitor and nonlinear inductor are defined as balanced [17].

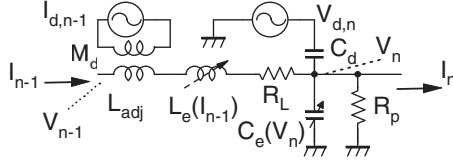


FIG. 5. Unit cell of the NLTL with duplex (V, I) driving and identical C_e and L_e nonlinearities. See Eq. (3). R_p is the parallel resistor of the capacitor, R_L is the series resistor of the inductor. The two driving terms for the duplex driver are balanced with the additional condition on the mutual inductance M_d given by Eq. (17).

B. Model 2, balanced duplex driver

The schematic electrical unit cell configuration that makes possible a duplex driver is presented in Fig. 5. As we shall see, this driving feature, when properly designed, can make the dissipative unit cell self-dual. For nonlinear balance, both $C_e(V)$ and $L_e(I)$ are to be balanced, so a linear L_{adj} is added in series to L_e as shown in Fig. 5. This allows one to maintain the unit cell balance via Eq. (3). Next we add to that condition the complex balancing possibility shown in Fig 5. This duplex driving involves both voltage driving via a capacitor and, simultaneously, current driving of the inductor in the unit cell via a separate driver and transformer. Now L_{adj} is used as the secondary winding, and the second oscillator is connected to the primary winding of the transformer, where M_d is the mutual inductance between those coils.

C. Self-dual NLTL

The dynamic equations of motion for the NLTL described by the unit cell in Fig. 5 are now

$$(L_e(I_n) + L_{adj}) \frac{dI_n}{dt} = V_n - V_{n+1} - I_n R_L + M_d \frac{d}{dt} I_{d,n}, \quad (7)$$

$$(C_e(V_n) + C_d) \frac{dV_n}{dt} = I_{n-1} - I_n - \frac{V_n}{R_p} + C_d \frac{d}{dt} V_{d,n}, \quad (8)$$

$$Z_0 \left(\frac{C_0}{\sqrt{1 + V_{n+0.5}^2/V_0^2}} + C_d \right) \frac{dV_{n+0.5}}{dt} = V_n - V_{n+1} - \frac{R_L}{Z_0} V_{n+0.5} + M_d I_d \frac{d}{dt} \cos(k_d(n+0.5) - \omega_d t), \quad (14)$$

$$Z_0 \left(\frac{C_0}{\sqrt{1 + V_n^2/V_0^2}} + C_d \right) \frac{dV_n}{dt} = V_{n-0.5} - V_{n+0.5} - \frac{Z_0}{R_p} V_n + Z_0 C_d V_d \frac{d}{dt} \cos(k_d n - \omega_d t), \quad (15)$$

where the damping terms are now balanced by the added condition that

$$R_L R_p = Z_0^2. \quad (16)$$

The driving terms are balanced for the duplex driver described by Eqs. (14) and (15) with the additional condition that

$$M_d I_d = Z_0 C_d V_d. \quad (17)$$

With the damping and drivers all balanced, Eqs. (14) and (15) become one. The result is a driven-damped, running ILM self-dual lattice problem.

where the parameters are identified in Fig. 5. Note the coefficient M_d in the driving term of the current, Eq. (7), can be different from L_{adj} .

Since the laboratory equations of motion include a driving capacitor C_d and adjustment inductor L_{adj} in Eqs. (7) and (8) the Eq. (3) balance condition including C_d and L_{adj} now becomes

$$\frac{L_{adj}}{L_0} = \frac{C_d}{C_0}. \quad (9)$$

From Eq. (6), we note the useful equalities with dimensions of (impedance)², namely,

$$Z_0^2 = \frac{V_0^2}{I_0^2} = \frac{L_0}{C_0} = \frac{L_0 + L_{adj}}{C_0 + C_d}. \quad (10)$$

For self-dual network lattices, one can introduce, without loss of generality, a new set of variables at half integer sites to replace the current variables [1], so

$$V_{n+0.5} = Z_0 I_n. \quad (11)$$

By this convention, these $V_{n+0.5}$ variables are essentially current data, but have the same variable name and dimension as the voltage variable. Similarly, with these two set of variables, the two synchronous drivers should have 1/2 position shift dependence given by

$$I_{d,n} = I_d \cos(k_d(n+0.5) - \omega_d t) \quad (12)$$

and

$$V_{d,n} = V_d \cos(k_d n - \omega_d t), \quad (13)$$

where I_d, V_d , are real number driving amplitudes. Note the duplex driver configuration, represented by Eqs. (12) and (13), requires two times the number of drivers previously used for the single driver cyclic experiments described in Sec. II.

The two equations of motion, Eqs. (7) and (8), become, respectively,

IV. SIMULATIONS AND RESULTS

A. Simulation details

It has already been demonstrated in Sec. II with experiments and simulations that for a running ILM in an unbalanced NLTL, a characteristic, strong resonant interaction signature between the ILM and NLTL modes can be clearly identified. The strength of this resonant interaction between the running ILM and the lattice modes determines the magnitude of the NLTL backwave, hence the localized mode-lattice mode coupling.

Table I(A) identifies the common parameters used in the present simulations. The nonlinear capacitor values are the same as described in Ref. [17]. C_d is set at an appropriate

TABLE I. Simulation parameters for balanced nonlinearities.

(A) Common values for the two models					
$C_0=117\text{nF}$	$V_0=4.24\text{V}$	$L_0=1.00\text{mH}$	$Z_0 = 92.4\Omega$		
$I_0=0.0459\text{A}$	$C_d=10.0\text{nF}$	$L_{\text{adj}} = 85.5\mu\text{H}$			
(B) Model numbers and parameter sets for Figs. 8 and 9					
Model 1 = single driver; model 2 = duplex driver					
No. Panel	Drive	$R_p(\Omega)$	$R_L(\Omega)$	$V_d(\text{V})$	$M_d I_d(\mu\text{HA})$
1, (a)			Eq. (16)		
Balanced R	V	776	11.0	30.0	
1, (b)					
Unbalanced R	V	1.55k	16.5	30.0	
2, (c)			Eq. (16)		Eq. (17)
Balanced R	V, I	776	11.0	15.0	13.9
2, (d)					Eq. (17)
Unbalanced R	V, I	1.55k	16.5	15.0	13.9

experimental value $\sim 1/10$ of C_0 . L_0 is chosen as the same as in Ref. [17]. I_0 and L_{adj} are calculated at the balanced condition. Table I(B) summarizes the parameter sets for different driving and damping conditions.

In these simulations, the fourth-order Runge-Kutta method is used in Eqs. (7) and (8) with parameters listed in Tables I(A) and I(B). Because of the driver dissipation conditions, initially, a single ILM is generated by chirping the driver frequency up starting from near the top of the dispersion curve (27.1kHz) to a higher frequency, typically 35 kHz, which is lower than the high-frequency driving limit of 60 kHz. If several traveling ILMs are obtained, then one uses zero filling at unwanted locations to eliminate all but one. A clean stable traveling ILM is generated after continuing the simulation beyond a couple of time constants. By increasing or decreasing the driver frequency and waiting until the extended waves have disappeared, we were able to investigate ILM amplitude, velocity, and ILM-DL as a function of the driver frequency.

The modulus amplitudes of the DL are calculated from the complex 2D-FT result for a fixed k by summing square amplitudes along the frequency axis across the DL with a fixed width (2 kHz) of data points, then taking the square root of the sum. The result is the DLS. The reason for taking a sum is because the DL is not exactly on the data points of discrete 2D data. Since the FT signal decays quickly moving away from the DL, the integrated width is not sensitive to the final results. See Appendix for more details.

B. Time-dependent properties of self-dual ILM

Particularly instructive are the numerical properties of the traveling, balanced self-dual ILM within a cell and we present some of these observations in Fig. 6, where identical ILM envelope shapes are observed at capacitively centered and inductively centered lattice locations. This example of simulation results, for a self-dual case, at $k_d = 13\pi/16$ and $\omega_d/2\pi = 50$ kHz with the balanced conditions for the damping resistors and drivers included, gives a single traveling ILM moving at a constant speed around the ring. The time dependence of the ILM voltage pattern in Fig. 6(a) is displayed in blue-white-red colors with the same definitions as

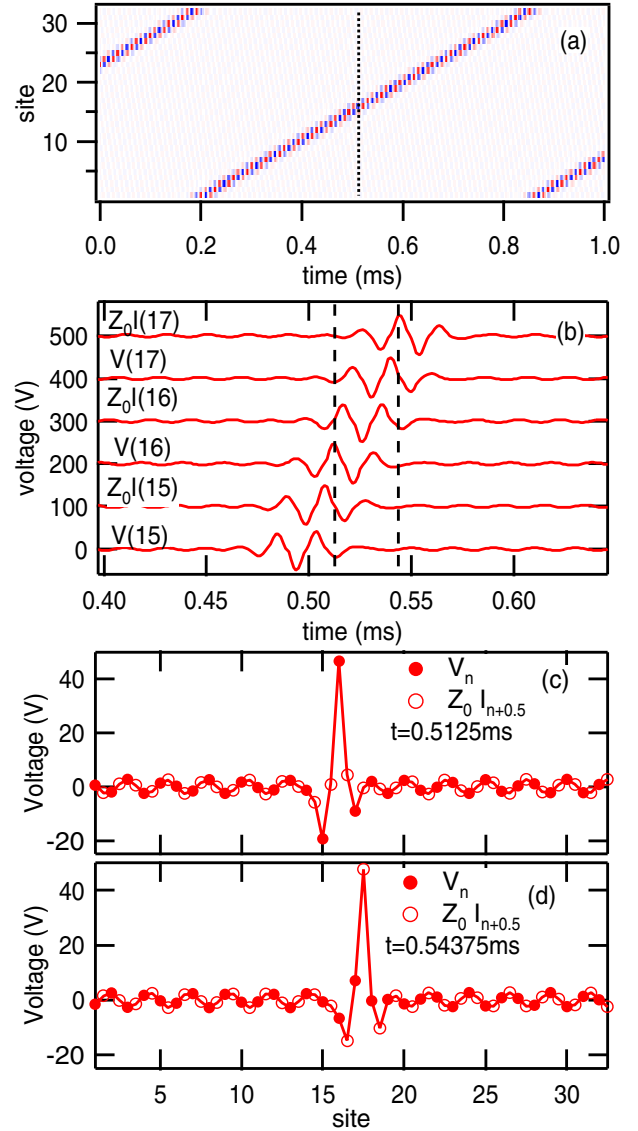


FIG. 6. A traveling, balanced self-dual ILM showing its identical envelope shape at capacitively centered and inductively centered lattice locations in a 32-element NTL ring. (a) Simulated voltage pattern versus time for a traveling ILM, driven at 50 kHz. Voltage pattern is shown in blue-white-red scale. (b) Time dependence of voltage and current for sites from 15 to 17. (c) Voltage and current as a function of lattice site at time = 0.5125 ms, identified by left dashed line in (b). Solid circles identify voltage at integer sites, and open circles identify current at half-integer sites. (d) Voltage and current as a function of lattice site at time identified by right vertical dashed line in (b). Peak is now at the current site. Peak distance between (c) and (d) is 1.5 lattice sites. See text for more details.

for Fig. 4(a). But, because of the new balance conditions, we want to examine the voltage and current pattern in more detail. (The vertical dotted line identifies the time = 0.5125 ms, to be referred to in the next two panels.)

Figure 6(b) illustrates the equivalency of $Z_0 I_n$ and $V_{n+0.5}$ expressed by Eq. (11) with the voltage and current excitation passing through neighboring cells, labeled (in parentheses) $n = 15$ to $n = 17$ versus time. $Z_0 I_n$ is the current in voltage units. Curves are shifted up for clarity with the lattice order as

indicated by Eq. (11). A near identical wave form is observed for both voltage V_n and current I_n multiplied by Z_0 . In addition, the center of the ILM shifts to the right uniformly across both voltage and current sites. The right vertical dashed line identifies the time of the particular ILM current maximum in cell (17), while the left vertical dashed line [also identified in panel (a)] identifies the time of the particular ILM voltage maximum in cell (16).

To better characterize the envelope shapes at capacitively centered and inductively centered lattice locations, the voltage and current signals in Figs. 6(c) and 6(d) are now plotted versus lattice site for two different times. These time points are chosen so voltage and current peaks are at different lattice points. Figure 6(c) (time = 0.5125 ms): Solid circles at integer sites are for voltages and open circles at half-integer sites are for currents multiplied by Z_0 . The voltage shows a maximum at site (16), while the current does not. Figure 6(d) (time = 0.54375 ms): Voltage and current as a function of lattice site at slightly later time than Fig. 6(c), identified by right vertical dashed line in Fig. 6(b). Here the peak is at the current site while in Fig. 6(c), the peak is at a voltage site. The time difference is about 1.56 cycles of vibration, and distance between the peaks in Figs. 6(c) and 6(d) is 1.5 lattice sites. Because the phase velocity and ILM velocity are not the same, the time difference between those two panels is not a multiple of the vibration period. Outside the ILM eigenpeak region, the extended background wave is observed, which is due to the drivers.

For completeness, we include an extended view of the 2D-FT of the running, balanced self-dual voltage pattern time-dependent results shown in Fig. 6(a). The resulting ILM DLS for the fundamental, the third harmonic, and fifth harmonic are presented in Fig. 7. The fundamental shows the intersection with the NLTL dispersion curve (see arrow). The intersections for the third and fifth harmonics with the NLTL are not shown. Like the experimental ILM-DL in Fig. 4(b), the cross indicates the driver wave number and frequency at the fundamental. The third harmonic and fifth harmonic DLs for the reduced zone are obtained from the simulation data in the standard way. The equation relating the fundamental dispersion line, DL(1) to its harmonic DL($2m + 1$), where $m = 0, 1, 2, 3, \dots$, is given by

$$f_{(2m+1)}(k) = \frac{v}{2\pi}(k - (2m + 1)k_d - G_m) + (2m + 1)f_d, \quad (18)$$

where v is the ILM velocity, $G_m = 2\pi m$ the reciprocal lattice wave number, and $f_d = \omega_d/(2\pi)$. Note the third-harmonic DL passes the point $(3k_d, 3f_d)$ (dotted cross) with the same slope as the fundamental DL. Since the wave number of the 2D-FT result in Fig. 7 is limited from $-\pi$ to π , by Eq. (18), the wave number of $3k_d = 39\pi/16$ in Fig. 7 appears at $3k_d = 39\pi/16 - 2\pi = 7\pi/16$. By the same reasoning, $5k_d = 65\pi/16$ for the fifth-harmonic DL appears at $5k_d = 65\pi/16 - 4\pi = \pi/16$. As expected, these harmonic DLs are much weaker than the fundamental one. This simulation of the fundamental ILM DL result (without a ghost) appears similar to the earlier experimental work, but as we shall show the resonant backwave results for the ILM fundamental are quantitatively different. The resonances associated with each of these harmonics is expected to be progressively weaker

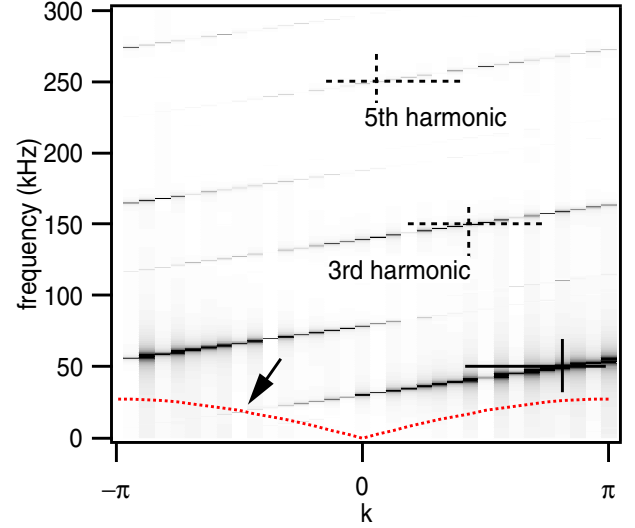


FIG. 7. 2D-FT of running, balanced self-dual ILM voltage pattern presented in Fig. 6(a). ILM DLS versus k and frequency is expressed by a gray scale. Solid cross identifies driving wave number $k_d = 13\pi/16$, frequency ($f_d = 50$ kHz) point. Dashed curve: NLTL linear dispersion curve. Arrow: Intersection point of the ILM DL and the NLTL dispersion curve. Running ILM to the right, NLTL backwave to the left. In this extended frequency figure, third harmonic and fifth harmonic ILM DLs are also seen. Dashed crosses are guides to eye, indicating third and fifth harmonic points of the (k_d, f_d) -driven ILM.

because of the much weaker harmonic DL signal compared to the fundamental. In addition, the wave number distance to the corresponding NLTL DL intersecting point is much farther removed. For these reasons, only the fundamental DL resonance is examined in what follows.

C. Simulation results for models 1 and 2

Following the same procedure as in experiments, the ILM-DL simulation results for models 1 and 2, at 50 kHz are now described. Because of the relatively weak backwave resonances for these Table I parameter sets, the observed ILM velocities are essentially the same, differing by less than 0.42%. Figure 8(a) presents model 1, log ILM-DL strength, over four orders of magnitude, versus wave number for capacitive driving. Balanced damping indicates that the circuit resistances satisfy the Eq. (16) condition. The up arrow identifies the driving point $k_d = 13\pi/16$ and the down arrow the ILM&NLTL resonance point. The solid curve V (red) is the ILM-DL voltage modulus and the dashed curve $Z_0 I$ (blue) is the follower current modulus response. Figure 8(b), model 1, displays a similar example for capacitive driving but now for unbalanced dissipation. In these two panels, asymmetric resonance signatures are clearly observed. The distortion is due to interference between the large amplitude ILM DL component and the small amplitude NLTL signal at the same frequency, a characteristic feature of a Fano resonance. Related Fano signatures already have been described for a stationary ILM interacting with small amplitude running waves [57,58].

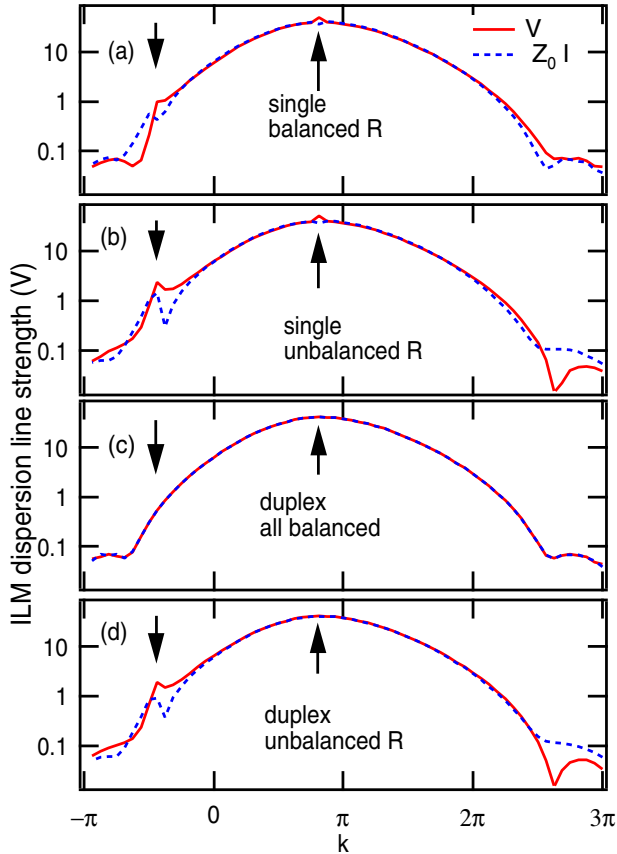


FIG. 8. ILM DLS of V (red) and $Z_0 I$ (blue) data for the single driven (model 1) and duplex driven (model 2) cases. Driving frequency 50 kHz. Up arrow, driving point: $k \uparrow = 13\pi/16$. Down arrows $k \downarrow = -1.39$, same location in the four frames, identify the intersection point of ILM DL and the NLTL dispersion curve. (a) Model 1, damping balanced. (b) Model (1), damping unbalanced. Nearby red and blue features show the actual resonance responses. (c) Model 2, damping balanced. (d) Model 2, damping unbalanced. No resonance features are observed for (c), the completely balanced self-dual model.

The next step is to examine the ILM-DL simulation results with a balanced duplex driver, i.e., when both V and I are driven simultaneously. These results for model 2 with balanced damping are present in Fig. 8(c). Here the running ILM voltage and current DLSs become identical, because Eqs. (14) and (15) are the same and the resonance strength is absent. No evidence of a resonant interaction between the ILM and the NLTL normal modes is evident at the crossing point, identified by the down arrow. Figure 8(d) presents the ILM-DL results for model 2 of Table I(B), where the unbalanced damping feature for the V and I drivers is introduced. Now the ILM-NLTL resonance interaction between the ILM and the NLTL reappears, with a strength similar to that found for the single driver cases. An important condition is the balancing of the dissipation. But clearly, it is Fig. 8(c) of model 2 that breaks new ground as the only configuration that removes the backwave, and hence, appears to uncouple the ILM from the NLTL modes.

To obtain a measure of the changes in the resonant behavior for the cases described here, it is helpful to examine a DLS

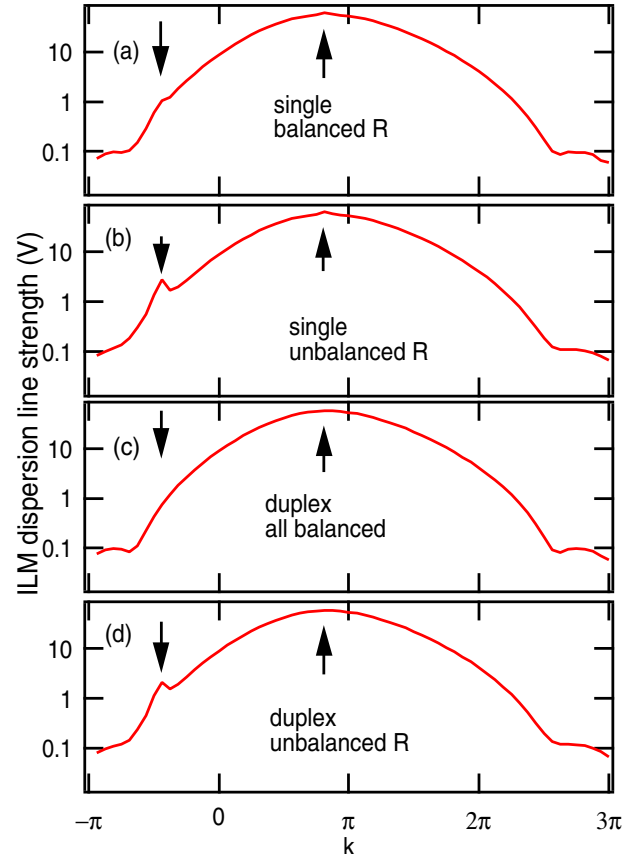


FIG. 9. Combined ILM DLS for the same eight sets of data presented in Fig. 8. Results calculated from Eq. (19), with Fig. 8 data: $|\tilde{V}(k)|$ and $|\tilde{I}(k)|$. A simple resonance feature is evident in three of the four panels.

function that incorporates both the voltage and current moduli, namely,

$$\text{DLS} = \sqrt{|\tilde{V}(k)|^2 + Z_0^2 |\tilde{I}(k)|^2} \quad (19)$$

These strength results are presented as a function of k in Figs. 9(a)–9(d), where only single resonant peaks appear in the final results.

To examine the relative strengths of the resonances for the different cases, we expand the down-arrow sections of Fig. 9, as now shown in Fig. 10, first in the panel (1) ordinate log plot, and then in the panel (2) ordinate linear plot. The vertical dashed lines in these two panels identify the region of interest. In panel (1), the curves labeled (a)–(d) are the same as shown in Fig. 9. Since the completely balanced self-dual case, dotted curve (c) shows no resonance, we subtract curve (c) from curves (b), (d), and (a) to obtain the resonance feature itself first in panel (2), Fig. 10. It is helpful to remember that all the simulation results are for a balanced nonlinear inductor and nonlinear capacitor. Given that restriction, it is interesting that although the completely balanced self-dual case appears to remove the coupling between the ILM and the NLTL, the next best case is for the single driver with balanced damping.

So far, only one driving frequency has been shown in Fig. 8. Figure 11 displays the ILM-DL in blue-white-red color scale, as a function of the driver frequency both for model

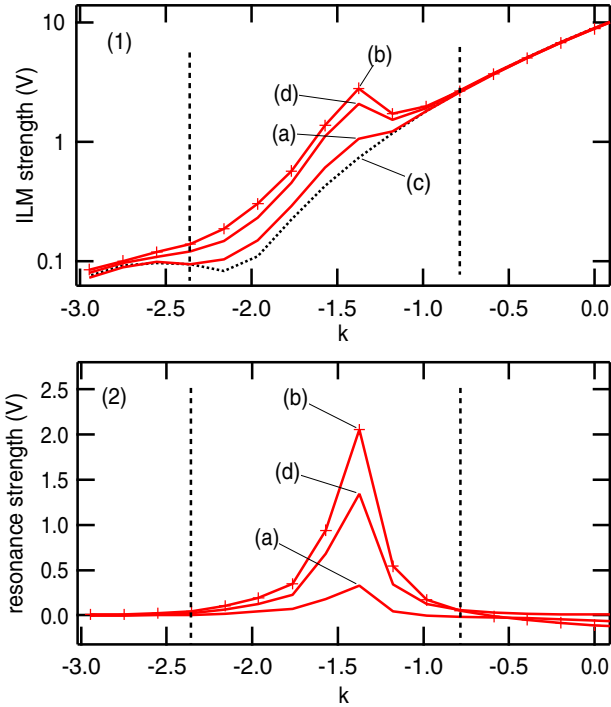


FIG. 10. Three examples of resonance strength suppression for balanced nonlinearities (data from Fig. 9). Panel (1), log ordinate. The dashed trace, model 2(c), shows no indication of a resonance and is used as the baseline in panel (2) to obtain the relative strengths of curves (b), (d), (a). Model 1(b): Largest resonance strength, single V driver with unbalanced damping. Model 2(d): Somewhat weaker, duplex driver with damping unbalanced. Model 1(a): Weakest resonance strength, single driver with balanced damping.

1 [unbalanced resistors and V driving, Fig. 8(b)]; and for model 2 [completely balanced, Fig. 8(c)]. Comparing these two panels demonstrates that over the entire ILM driving range, no resonance is observed for the completely balanced case, shown in Fig. 11(b), while a resonance response remains over the entire driving frequency range for the unbalanced case in Fig. 11(a).

Additional dissipation studies reveal that no resonance feature for the balanced self-dual NLTL is observed over a wide range of the damping, from a factor of 1/100 to 2. (Note: The driving amplitude is changed in proportion to the damping factor.) For the single driving NLTL case presented in Fig. 8(a), and for the unbalanced damping cases in Figs. 8(b) and 8(d), the resonance strength increases with increased damping. The exception in Figs. 8(b) and 8(d) is for the lowest damping case of 1/100, where the NLTL cannot support a traveling ILM.

V. SUMMARY AND CONCLUSIONS

In this study of backwave generation by a running ILM in balanced cyclic 1D NLTL transmission lines, a number of features have been studied for both balanced and unbalanced dissipative and driving conditions in the discrete lattice limit. They are listed here.

(1) The resonance generating the fundamental backwave from the ILM is relatively large when a single unit cell

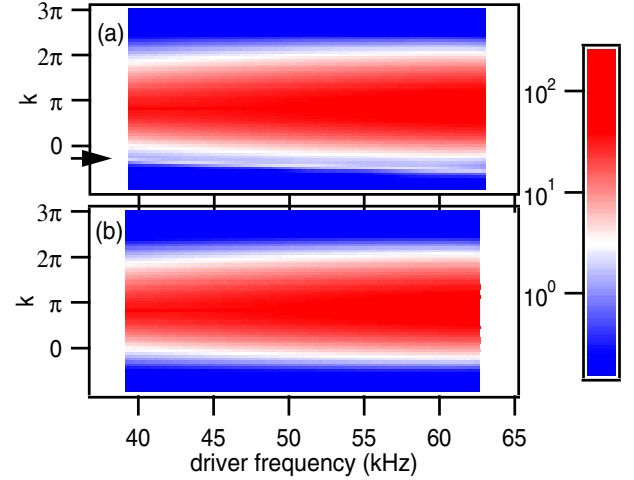


FIG. 11. ILM-DL strength as a function of wave number and driver frequency. Logarithmic strength is displayed by red-white-blue color. For the unbalanced resistors and capacitive driving case (model 1) panel (a), resonance response (horizontal arrow) is observed at all frequencies. For the all balanced duplex (V , I) driver case (model 2) shown in (b), no resonance signal is observed over the same wide driving frequency range.

driver is used together with either a nonlinear capacitor NLTL, a nonlinear inductor NLTL, or an unbalanced nonlinear capacitor or nonlinear inductor NLTL in a dissipative system.

(2) With the single cell driver, the fundamental backwave resonance is greatly reduced, but still observable, when the nonlinear capacitor and nonlinear inductor are balanced in the NLTL, according to Eq. (3). Given this condition, additional ways have been discovered with which to suppress the remaining fundamental resonance feature.

(3) Adding to (2) the balancing of the dissipation between the capacitive and inductive parts of the cell, Eq. (16), produces the next large decrease in the fundamental resonance behavior.

(4) The key to completely removing the fundamental backwave is the introduction of the balanced Eq. (17) duplex driver. The important findings, presented in Figs. 8(c) and 9(c) occur when all terms, including the traveling wave duplex (V , I) driver, are balanced, so the dynamical voltage and current equations of motion become the same, resulting in a damped, driven self-dual NLTL.

(5) The absence of an ILM-generated fundamental backwave for the damped, driven self-dual NLTL is independent of the steady-state driving frequency.

(6) Although the fundamental resonance is eliminated, it is important to remember that the much weaker higher harmonic resonances still exist and have not been characterized in this paper. We emphasize that this elimination of the fundamental backwave resonance is only possible in the NLTL with a balanced duplex driver, not a balanced single driver.

A different way to visualize this interesting study of backwave control is to contrast the result with that of a running ILM for the customary traveling-wave (V) driver presented in Fig. 4 for an unbalanced NLTL. In the unbalanced case, the traveling ILM periodically changes its shape between

capacitive-centered and inductive-centered locations in the unit cell. On the other hand, with the necessary balanced duplex driver, as demonstrated in Fig. 6, the resulting identical capacitive-centered and inductive-centered equations developed here demonstrate no difference between the fundamental ILM envelope shapes at these two locations. The result is that the traveling ILM is uncoupled from the NLTL modes so no fundamental resonance or associated backwave is to be expected or observed. Only the very weak higher harmonic resonances between the ILM and the NLTL remain.

Our recipe for the production of a nearly distortion-free, running, localized energy pulse in a dissipative, 1D NLTL has been demonstrated. The result is the elimination of the fundamental backwave, a characteristic feature of a periodic 1D lattice. As long as the discrete, site and bond (intersite) dissipative, dynamical, nonlinear equations can be made self-dual, which necessarily requires a duplex driver, the exact nonlinear functional form of the NLTL does not appear to

matter. This degree of uncoupling of the localized excitation from the extended waves is not possible with a single unit cell driver, which has been used in all previous NLTL studies.

ACKNOWLEDGMENTS

M.S. is supported by Grant-in-Aid for JSPS KAKENHI Grant No. JP25400394. A.J.S. is supported by a Podell Endowment Award for Research and Scholarship.

APPENDIX: DEVELOPMENT OF THE DISPERSION LINE STRENGTH (DLS) FROM THE ILM VOLTAGE MEASUREMENT

For a voltage pattern $V(t = m\Delta t, z = n) = V'(m, n)$, where m and n are integer numbers for the data and Δt is a sampling time, 2D-FT is calculated as

$$\begin{aligned}\tilde{V}'(p, q) &= \sum_{m=0, n=0}^{M-1, N-1} V'(m, n) \exp\left(2\pi i \frac{p}{M\Delta t} m\Delta t\right) \exp\left(-2\pi i \frac{nq}{N}\right) \\ &= \sum_{m=0, n=0}^{M-1, N-1} V'(m, n) \exp(ip\Delta\omega \times m\Delta t - iq\Delta k \times n),\end{aligned}\quad (\text{A1})$$

where p and q are integers corresponding to frequency and wave number. The frequency step and wave-number step are $\Delta\omega = \frac{2\pi}{M\Delta t}$ and $\Delta k = \frac{2\pi}{N}$. Lattice size $N = 32$ and time data number $M = 8192$ for experiments and 320 000 for simulations. The sampling frequency is 250 kHz for experiments and 800 kHz for simulations. These values are proportional to the number of data points for time M . However, it doesn't depend on lattice size N , as long as the ILM number is one, because the ILM width doesn't depend on the lattice size. Thus, we define

$$\tilde{V}(\omega = \Delta\omega p, k = \Delta k q) = \frac{\tilde{V}'(p, q)}{M} \quad (\text{A2})$$

for the dispersion voltage for one ILM.

To calculate FT strength along the DL, we sum the modulus amplitude along the frequency axis because the

DL doesn't pass exactly on the frequency points $\omega = \Delta\omega \times p$. The summing is made from $p_{\text{DL}} - \delta$ to $p_{\text{DL}} + \delta$, where $p_{\text{DL}} = \text{floor}(\frac{\omega_{\text{DL}}}{\Delta\omega})$, $\omega_{\text{DL}} = v(k - k_d) + \omega_d$, and $2\delta = (2\pi f_r)/\Delta\omega$, where f_r is the frequency range. This frequency range is wider than the line width to accumulate the DLS and narrow enough to avoid detecting other signals. It is 3 kHz for experiments and 2 to 3 kHz for simulations. The final expression for the DLS is

$$|\tilde{V}(k = \Delta k q)| = \frac{\sqrt{\sum_{p=p_{\text{DL}}-\delta}^{p_{\text{DL}}+\delta} |\tilde{V}'(p, q)|^2}}{M}. \quad (\text{A3})$$

Equation (A3) corresponds to a 1D FT of the envelope function in real space. The unit is volts for both $\tilde{V}(\omega, k)$ and $|\tilde{V}(k)|$.

-
- [1] R. Hirota and K. Suzuki, *J. Phys. Soc. Jpn.* **28**, 1366 (1970).
[2] K. Fukushima, M. Wadati, and Y. Narahara, *J. Phys. Soc. Jpn.* **49**, 1593 (1980).
[3] D. N. Christodoulides and R. I. Joseph, *Opt. Lett.* **13**, 794 (1988).
[4] B. A. Malomed, *Phys. Rev. A* **45**, 4097 (1992).
[5] T. Kuusela, J. Hietarinta, and B. A. Malomed, *J. Phys. A: Math. Gen.* **26**, L21 (1993).
[6] M. Sato, B. E. Hubbard, A. J. Sievers, B. Ilic, D. A. Czaplowski, and H. G. Craighead, *Phys. Rev. Lett.* **90**, 044102 (2003).
[7] M. Sato and A. J. Sievers, *Nature (London)* **432**, 486 (2004).
[8] J. P. Wrubel, M. Sato, and A. J. Sievers, *Phys. Rev. Lett.* **95**, 264101 (2005).
[9] E. Kenig, B. A. Malomed, M. C. Cross, and R. Lifshitz, *Phys. Rev. E* **80**, 046202 (2009).
[10] N. Boechler, G. Theocharis, S. Job, P. G. Kevrekidis, M. A. Porter, and C. Daraio, *Phys. Rev. Lett.* **104**, 244302 (2010).
[11] F. Palmero, L. Q. English, J. Cuevas, R. Carretero-González, and P. G. Kevrekidis, *Phys. Rev. E* **84**, 026605 (2011).
[12] W. Shi, S. Shige, Y. Soga, M. Sato and A. J. Sievers, *Europhys. Lett.* **103**, 30006 (2013).
[13] M. Kimura, Y. Matsushita, and T. Hikihara, *Phys. Lett. A* **380**, 2823 (2016).

- [14] F. Palmero, L. Q. English, X.-L. Chen, W. Li, J. Cuevas-Maraver, and P. G. Kevrekidis, *Phys. Rev. E* **99**, 032206 (2019).
- [15] F. Palmero, J. Cuevas-Maraver, L. Q. English, W. Li, and R. Chacón, *Phys. Scr.* **94**, 065210 (2019).
- [16] Y. Watanabe, T. Nishida, Y. Doi, and N. Sugimoto, *Phys. Lett. A* **382**, 1957 (2018).
- [17] M. Sato, H. Furusawa, M. Sakai, Y. Soga, and A. J. Sievers, *Chaos* **32**, 033118 (2022).
- [18] M. Toda, *Theory of Nonlinear Lattices* (Springer Verlag, New York, 1989).
- [19] M. J. Ablowitz and J. F. Ladik, *J. Math. Phys.* **16**, 598 (1975).
- [20] R. Hirota, *J. Phys. Soc. Jpn.* **35**, 289 (1973).
- [21] M. M. Bogdan and D. V. Laptev, *J. Phys. Soc. Jpn.* **83**, 064007 (2014).
- [22] S. Aubry, *Physica D* **103**, 201 (1997).
- [23] S. Aubry, *Physica D* **216**, 1 (2006).
- [24] S. Flach and C. Willis, *Phys. Rep.* **295**, 181 (1998).
- [25] A. S. Dolgov, *Fiz. Tverd. Tela* **28**, 1641 (1986) [*Sov. Phys. Solid State* **28**, 907 (1986)].
- [26] A. J. Sievers and S. Takeno, *Phys. Rev. Lett.* **61**, 970 (1988).
- [27] J. B. Page, *Phys. Rev. B* **41**, 7835 (1990).
- [28] D. Bonart, T. Rössler, and J. B. Page, *Phys. Rev. B* **55**, 8829 (1997).
- [29] D. Bonart, T. Rössler, and J. Page, *Physica D* **113**, 123 (1998).
- [30] T. Rössler and J. B. Page, *Phys. Rev. B* **62**, 11460 (2000).
- [31] T. Kuusela, *Chaos, Solitons & Fractals* **5**, 2419 (1995).
- [32] A. J. Sievers and J. B. Page, in *Phonon Physics: The Cutting Edge*, Dynamical Properties of Solids, Vol. 7, edited by G. K. Horton and A. A. Maradudin (Elsevier, Amsterdam, 1995), pp. 137–259.
- [33] M. Remoissenet, *Waves Called Solitons: Concepts and Experiments* (Springer-Verlag, Berlin, 1999).
- [34] A. Scott, *Nonlinear Science: Emergence and Dynamics of Coherent Structures* (Oxford University Press, New York, 1999).
- [35] D. K. Campbell, S. Flach, and Y. S. Kivshar, *Phys. Today* **57**(1), 43 (2004).
- [36] M. Sato, B. E. Hubbard, and A. J. Sievers, *Rev. Mod. Phys.* **78**, 137 (2006).
- [37] S. Flach and A. V. Gorbach, *Phys. Rep.* **467**, 1 (2008).
- [38] A. J. Fairbanks, A. M. Darr, and A. L. Garner, *IEEE Access* **8**, 148606 (2020).
- [39] M. Sato, M. Sakai, and A. J. Sievers, in *13th Chaotic Modeling and Simulation*, edited by C. H. Skiadas and Y. Dimotikalis, Springer Proc. in Complexity (Springer, Switzerland, 2021), pp. 783–796.
- [40] E. Kengne, W.-M. Liu, L. Q. English, and B. A. Malomed, *Phys. Rep.* **982**, 1 (2022).
- [41] J. Gómez-Gardeñes, L. M. Floría, M. Peyrard, and A. R. Bishop, *Chaos* **14**, 1130 (2004).
- [42] J. Gómez-Gardeñes, F. Falo, and L. Floría, *Phys. Lett. A* **332**, 213 (2004).
- [43] K. Yoshimura and Y. Doi, *Wave Motion* **45**, 83 (2007).
- [44] M. Sato, T. Nakaguchi, T. Ishikawa, S. Shige, Y. Soga, Y. Doi, and A. J. Sievers, *Chaos* **25**, 103122 (2015).
- [45] K. W. Sandusky, J. B. Page, and K. E. Schmidt, *Phys. Rev. B* **46**, 6161 (1992).
- [46] S. Flach and C. R. Willis, *Phys. Rev. Lett.* **72**, 1777 (1994).
- [47] D. Cai, A. R. Bishop, and N. Grønbech-Jensen, *Phys. Rev. Lett.* **72**, 591 (1994).
- [48] M. Kimura and T. Hikiyama, *Phys. Lett. A* **372**, 4592 (2008).
- [49] L. Hadžievski, A. Maluckov, M. Stepić, and D. Kip, *Phys. Rev. Lett.* **93**, 033901 (2004).
- [50] O. F. Oxtoby and I. V. Barashenkov, *Phys. Rev. E* **76**, 036603 (2007).
- [51] A. Shelkan, M. Klopov, and V. Hizhnyakov, *Phys. Lett. A* **383**, 1893 (2019).
- [52] Y. Doi and K. Yoshimura, *Phys. Rev. Lett.* **117**, 014101 (2016).
- [53] L. L. Bonilla and B. A. Malomed, *Phys. Rev. B* **43**, 11539 (1991).
- [54] J. L. Marín, F. Falo, P. J. Martínez, and L. M. Floría, *Phys. Rev. E* **63**, 066603 (2001).
- [55] D. Zueco, P. J. Martínez, L. M. Floría, and F. Falo, *Phys. Rev. E* **71**, 036613 (2005).
- [56] M. Johansson, J. E. Prilepsy, and S. A. Derevyanko, *Phys. Rev. E* **89**, 042912 (2014).
- [57] S. Flach, A. E. Miroshnichenko, V. Fleurov, and M. V. Fistul, *Phys. Rev. Lett.* **90**, 084101 (2003).
- [58] A. E. Miroshnichenko, S. Flach, and Y. S. Kivshar, *Rev. Mod. Phys.* **82**, 2257 (2010).